IJMMM International Journal of Minerals, Metallurgy and Materials 矿物冶金与材料学报（英文版）

Understanding the local structure and thermophysical behavior of Mg–La liquid alloys via machine learning potential

Jia Zhao, Taixi Feng, and Guimin Lu

Cite this article as:
Jia Zhao, Taixi Feng, and Guimin Lu, Understanding the local structure and thermophysical behavior of Mg–La liquid alloys via machine learning potential, *Int. J. Miner. Metall. Mater.*, 32(2025), No. 2, pp. 439-449. https://doi.org/10.1007/s12613-024-2928-2

View the article online at SpringerLink or IJMMM Webpage.

INTERNATIONAL JOURNAL OF
Minerals, Metallurgy and Materials

Volume 32, Number 2, February 2025
Page 439

Research Article https://doi.org/10.1007/s12613-024-2928-2

Understanding the local structure and thermophysical behavior of Mg–La liquid alloys via machine learning potential

Jia Zhao[1,2], *Taixi Feng*[1,2], *and Guimin Lu*[1,2)✉]

1) National Engineering Research Center for Integrated Utilization of Salt Lake Resource, East China University of Science and Technology, Shanghai 200237, China

2) Joint International Laboratory for Potassium and Lithium Strategic Resources, East China University of Science and Technology, Shanghai 200237, China

(Received: 9 February 2024; revised: 7 April 2024; accepted: 6 May 2024)

Abstract: The local structure and thermophysical behavior of Mg–La liquid alloys were in-depth understood using deep potential molecular dynamic (DPMD) simulation driven via machine learning to promote the development of Mg–La alloys. The robustness of the trained deep potential (DP) model was thoroughly evaluated through several aspects, including root-mean-square errors (RMSEs), energy and force data, and structural information comparison results; the results indicate the carefully trained DP model is reliable. The component and temperature dependence of the local structure in the Mg–La liquid alloy was analyzed. The effect of Mg content in the system on the first coordination shell of the atomic pairs is the same as that of temperature. The pre-peak demonstrated in the structure factor indicates the presence of a medium-range ordered structure in the Mg–La liquid alloy, which is particularly pronounced in the 80at% Mg system and disappears at elevated temperatures. The density, self-diffusion coefficient, and shear viscosity for the Mg–La liquid alloy were predicted via DPMD simulation, the evolution patterns with Mg content and temperature were subsequently discussed, and a database was established accordingly. Finally, the mixing enthalpy and elemental activity of the Mg–La liquid alloy at 1200 K were reliably evaluated, which provides new guidance for related studies.

Keywords: magnesium–lanthanum liquid alloys; local structure; macroscopic properties; thermodynamic behavior; deep potential molecular dynamic simulation

1. Introduction

The addition of lanthanum (La) to magnesium (Mg) alloys could enhance their performance, including increasing the Mg alloy's corrosion resistance [1], regulating their grain growth, and enhancing their mechanical properties [2–3], etc., thus boosting the product level of Mg alloys and improving their competitiveness in applications such as 3C products [4], the automotive industry [5], and the aerospace industry [6].

The properties of the melt metal determine the process of filling the casting and the physical–chemical processes during crystallization, and are therefore fundamental to the quality of castings. The structural, physical, and thermodynamic behavior of metals in the liquid state are intimately linked to the structure of their solid state. Thus, without a comprehensive understanding of the melt, it is impossible to achieve high-quality castings with optimum performance at a minimum cost. On the other hand, thermophysical descriptions of the Mg–La alloy are essential for revealing its chemical behavior and physical properties [7]. Therefore, an in-depth understanding of the local structure and thermophysical behavior of melt alloys could facilitate the identification of the optimum solidification process to produce a well-performing material, promoting the development of related industries. Although metal melts have been analyzed by experimental techniques such as high-temperature X-ray diffraction [8–9] and synchrotron radiation experiments [10–11], the experimental investigation of melts encounters plenty of challenges, such as the complexity of high-temperature tests and their high sensitivity to external perturbations. Fortunately, computational simulation sheds light on this dilemma.

Classical molecular dynamics (CMD) simulations are computationally efficient, but their accuracy depends on the potential model, while ab initio molecular dynamics (AIMD) is accurate but computationally intensive. The dilemma of accuracy and efficiency plagued molecular simulations until the advent of machine learning potentials. As a prominent representative, deep potential molecular dynamics (DPMD) has been widely adopted since its introduction, involving various application scenarios [12–18]. The investigation of the Mg–Al–Si alloy system [19] has shown that DPMD simulation is approximately a thousand times faster than AIMD simulation, and its computational cost is linearly related to the number of atoms in the system. As a result, DPMD simulation has been widely applied to alloy systems. Xu *et al.* [20]

✉ Corresponding author: Guimin Lu E-mail: gmlu@ecust.edu.cn

developed the deep potential (DP) model for crystalline and amorphous Li–Si alloys with different Li/Si ratios, discussed the structural and kinetic properties, and predicted the densities, partial radial distribution functions (RDF), and diffusion coefficients for the systems. Wang *et al.* [21] discussed the structural features and kinetic properties for Nb_5Si_3 alloys, as well as the atomic structures of normal and supercooled liquid Nb_5Si_3 using DPMD simulation. Based on the Voronoi polyhedral analysis, the atomic structure in the melting process was explored, and the mechanism of cluster evolution was derived. For the $Pd_{82}Si_{18}$ and $Pd_{75}Si_{25}$ liquid systems [22], it was demonstrated that the generated DP model is more accurate than embedded atom interatomic potential based on the analysis for RDF of atom pairs at 1600 K. Al-based alloys, such as Al–Tb alloy, Ti–Al alloy, and Al–Cu–Ni alloy, were thoroughly explored by DPMD simulation. Zhai and Wang [23] explored the local structure and nucleation processes of Ti–Al systems. Moreover, the nucleation mechanism and transformation process under high undercooling conditions were discussed. Ryltsev and Chtchelkatchev [24] developed the machine-learning interatomic potential for multicomponent Al–Cu–Ni melts, investigated the effect of different hyperparameter settings of the neural network, and obtained the best-performing potential model, after which the structural and kinetic properties of the system were then discussed. Tang *et al.* presented insights into the $Al_{90}Tb_{10}$ [25] and $Al_{90}Ce_{10}$ [26] alloys and analyzed their short-range ordering and the supercooled liquids. DPMD simulations have been also applied to the Mg-based alloys. He *et al.* [27] discussed the formation energies of various binary magnesium alloys, including Mg–La alloys. Wang *et al.* [28] investigated in-plane domain structures, interstitial atomic transitions, and out-of-plane stacking sequences of the Mg–Zn–Y ternary alloys. Zhu *et al.* [19] developed a DP model for the Mg–Al–Si alloy and discussed the alloy system's equations of state, lattice constants, shear modulus, and bulk modulus. For the Al–Cu–Mg alloy across the entire concentration range, Jiang *et al.* [29] trained a DP model, which describes the fundamental energetic and mechanical properties of the system with DFT (density functional theory) accuracy. With the DP model, Wang *et al.* [30] and Li *et al.* [31] realized the prediction of the crystal structures of the Al–Mg system and Al_2CuMg alloys, respectively.

The lack of understanding of the local structure and thermophysical behavior of Mg–La alloys has hindered their development. In this work, the Mg–La liquid alloys were in-depth understood using DPMD simulation driven by machine learning, providing theoretical guidance to optimize the manufacturing process and improve the alloy's properties.

2. Methodology

The whole computational procedure is divided into three parts. The first one is to perform AIMD simulations, whose results are then used as an initial dataset for the second stage. The second stage is devoted to exploration, enriching the phase space and constructing potential energy surfaces that accurately describe the atomic interaction forces. Finally, the well-trained DP model has been applied to simulate large-scale Mg–La liquid alloys over a long period of time to analyze their local structure and thermophysical behavior.

All AIMD simulations were driven by the Vienna Ab Initio Simulation Package (VASP 5.4.4) [32] with a plane wave basis at a 400-eV cut-off energy. The interaction between the nucleus and the inner electrons was handled by the Projector Augmented Wave (PAW) [33]. The exchange of electrons and the description of the associated interactions were described through the PBE method based on the Generalized Gradient Approximation (GGA) [34]. For the Mg–La liquid alloy, the wave function of the valence electrons was chosen to be $Mg(3s^2)$, $La\_s(4p5s^26d^1)$. The dispersion correction term was introduced into the system using Grimme's DFT-D3 method [35] with a zero-damping function. A $1 \times 1 \times 1$ *k*-point grid was applied, and for the energy convergence, it was set to 10^{-5} eV. All the AIMD simulations were conducted at a temperature of 1800 K for 6 ps with a 2-fs time step. The Mg–La liquid alloy system was thoroughly understood via seven components with varying compositions of Mg and La, whose detailed information is shown in Table 1. Initial configurations for all samples were constructed based on experimental densities using the Materials Studio (MS) software package.

Table 1. Atom number (*N*) of seven different compositions of Mg–La liquid alloys employed for AIMD simulations

Sample	Mg / at%	*N*(Mg)	*N*(La)	Total number
S1	0	0	100	100
S2	20	20	80	100
S3	40	40	60	100
S4	50	50	50	100
S5	60	60	40	100
S6	80	80	20	100
S7	100	100	0	100

The exploration of phase space is realized by the Deep Potential Generator (DP-GEN) workflow framework [36], which is divided into three parts: training, exploration, and labelling. The AIMD results were employed as the initial dataset for training to generate the initial DP model. This was implemented using the DeepMD kit (2.1.3) [37] driven by machine learning. The hyperparameter settings during the training process were consistent with the reference [17], only differing in the cut-off radius, which was defined as 6 Å for the Mg–La alloy system. Four DP models would be generated for each training procedure based on the different random seed numbers. During the training process, the atomic coordinates are mapped to the energy of the system by encoding and fitting networks. The Adam stochastic gradient descent method is employed to optimize the network weights, minimize the loss function (Eq. (1)), and generate the DP model. For more detail, please refer to the literature [38].

$$L(p_E, p_F) = p_E \Delta E^2 + \frac{p_F}{3N} \sum_i |\Delta F_i|^2 \quad (1)$$

where L is the sum of the root mean square errors (RMSE) of energy and force, i represents the ith atom, F denotes RMSE in force, p_E and p_F are adjustable prefactors representing energy (E) and force, respectively, with starting and ending values (0.02, 1) and (1000, 1).

The exploration process was performed in the Large-scale Atomic/Molecular Massively Parallel Simulator (LAMMPS) [39] compiled with the DP module. The first few iterations were conducted in the NVT ensemble as the potential energy surface was not accurate enough in the beginning, after which the simulation was switched to the NPT ensemble exploration. The different temperatures, covering 1200 to 1800 K with 200 K intervals, were investigated to explore the temperature evolution of the local structure and thermodynamic behavior. Four different pressures, including 0, 10^6, 10^7, and 10^8 Pa, were considered to enrich the phase space. The exploration time was initially set at 2 ps and was then increased and stabilized at 6 ps. During the exploration, the force information obtained from the four DP models was recorded, and the maximum force error ($\sigma_F^{\max}$) was thus deduced through Eq. (2), which will be used to determine whether the corresponding configuration is labeled for single-point energy calculations. The criterion for evaluation is the predetermined force error range [σ_{low}, σ_{high}]. If $\sigma_F^{\max} < \sigma_{\text{low}}$, it is considered that the existing DP model could accurately describe the configuration. $\sigma_F^{\max} > \sigma_{\text{high}}$ implies that the configuration may be unphysical. These two scenarios do not contribute to the DP model improvement and are not sent to the labeling stage for subsequent calculations. When the maximum force error of the configuration satisfies $\sigma_{\text{low}} < \sigma_F^{\max} < \sigma_{\text{high}}$, it would be collected as a candidate. In this work, σ_{low} was set based on the RMSE of the force in the DP-test results, and σ_{high} was set at 0.2 eV/Å.

$$\sigma_F^{\max} = \max \sqrt{\langle \| F_{w,i}(R_t) - \langle F_{w,i}(R_t) \rangle \|^2 \rangle} \quad (2)$$

$$\langle F_{w,i}(R_t) \rangle = \frac{1}{N_m} \sum_{j=1}^{N_m} F_{w,j,i}(R_t) \quad (3)$$

where $F_{w,i}(R_t)$ represents the force on the atom indexed i, w represents the parameters of the DP model, R_t denotes the configurations generated during exploration with t denoting a continuous or discrete operation. <> is the average of the model prediction, and N_m denotes the number of DP models, which is 4 in this work.

As for the labeling stage, all collected configurations were subjected to single-point energy calculations via the VASP package, with input parameters similar to those of the AIMD simulations. The energy and force data calculated for all candidate configurations were included in the training data for the next iteration. The DP-GEN task is regarded as having converged when the accuracy of three consecutive iterations in the exploration stage is higher than 99%. All data sets were then collected during the iteration process, and 1 million gradient descent training steps were implemented to generate the final DP model.

The DPMD simulation was performed within LAMMPS, whose system contains 10 times more atoms than that of AIMD, i.e., 1000 atoms. The Mg–La liquid alloy was first run through the NPT ensemble for 1 ns, and the equilibrium volume was derived from the average results of the last 400 ps, which was used to evaluate the density. The equilibrium configuration and average volume derived from the NPT ensemble were then applied to 1 ns of the NVT ensemble simulation. The local structure of the Mg–La alloy was analyzed from trajectory data with the R.I.N.G.S. code [40]. The energy data from the NVT ensemble was collected to assess the thermodynamic behavior.

3. Results and discussion

3.1. DP model performance

The accuracy of the trained DP model was evaluated through several aspects, including RMSEs, energy and force data, and structural information comparison results. Table 2 shows the RMSEs for all compositions of the Mg–La liquid alloy. It is shown that the maximum RMSEs of energy is 6.70 meV/atom, while for force, it is 0.14 eV/Å. The RMSE results for each Mg–La system illustrate that the trained DP model predicts energy and force better for Mg-rich systems (e.g., S6 and S7) than for La-rich systems (e.g., S1 and S2). This phenomenon shows that the trained DP model outperforms La in predicting energy and force for Mg. The RMSEs for the Mg–La alloy are close to those for the Li–Si [20], Ti–Al [23], and Al–Tb [25] systems, indicating that the DP model is reliable.

Table 2. RMSEs for all compositions of Mg–La liquid alloys

Sample	RMSE-energy / (meV·atom^{-1})	RMSE-force / (eV·Å^{-1})
S1	6.70	0.14
S2	5.27	0.13
S3	5.30	0.12
S4	4.71	0.12
S5	4.54	0.11
S6	2.86	0.08
S7	2.89	0.07

Fig. 1 shows the comparison results of energy and force in a random pickup from the test sets of the S4 system. The horizontal coordinate represents the energy and force calculated based on the DFT framework, while the vertical coordinate represents the corresponding energy and force information predicted by the trained DP model. It is found that the test results for energy and force are evenly distributed along the diagonal. The RMSE of energy and force in the S4 system is 4.71 meV/atom and 0.12 eV/Å, respectively, suggesting that the well-trained DP model could provide a good description of energy and force.

The RDF and the partial structure factor obtained from the DPMD simulation were compared with those reported in the publication. These comparison results were employed to fur-

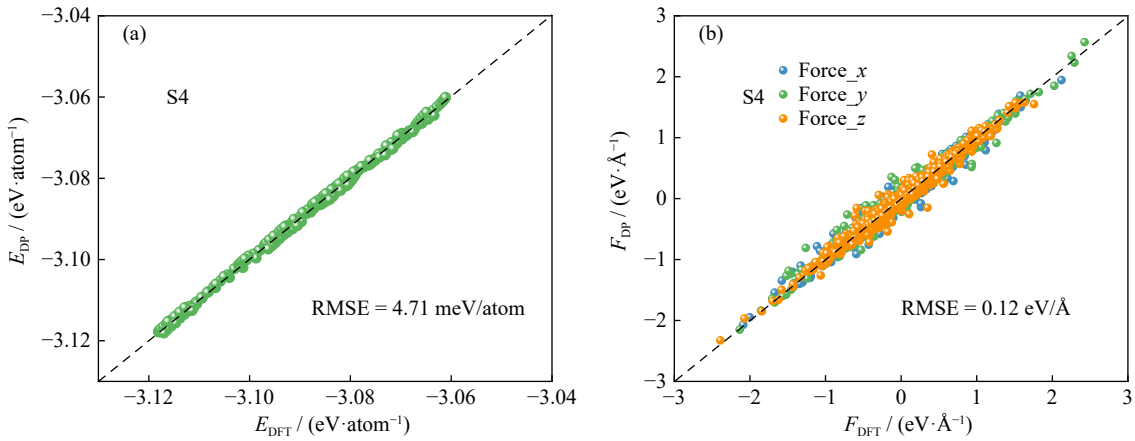

Fig. 1. Comparison of (a) energy (*E*) and (b) (*F*) force predicted by the DP model with the DFT result.

ther demonstrate the robustness of the trained DP model. Fig. 2 shows the comparison of the RDF and structure factor ($S(\boldsymbol{q})$) obtained for the S1 and S7 samples at 1200 K with those obtained by Dalgic *et al.* [41] and Wax *et al.* [42] at 1243 K and 953 K, respectively. For the S1 system, the RDF and $S(\boldsymbol{q})$ agree well with Dalgic *et al.*'s results [41] obtained from class molecular dynamic simulation, both in peak height and position. As for the S7 system, the RDF and $S(\boldsymbol{q})$ derived from the DPMD simulation at 1200 K were compared with the report of Wax *et al.* [42] using an analytic pair potential simulation. The overall trend and peak positions match well, with a little difference in peak heights. This is attributed to the differences in the temperatures studied, with higher peak intensities at lower temperature, which will be explained in the subsequent discussion. All these comparisons suggest that the well-trained DP model is sufficient to understand the local structure and thermophysical behavior of Mg–La liquid alloys.

3.2. Local structure analysis

3.2.1. Partial radial distribution function

The local structure of the Mg–La liquid alloy was evaluated by the RDF, whose mathematical expression is shown in Eq. (4) [43].

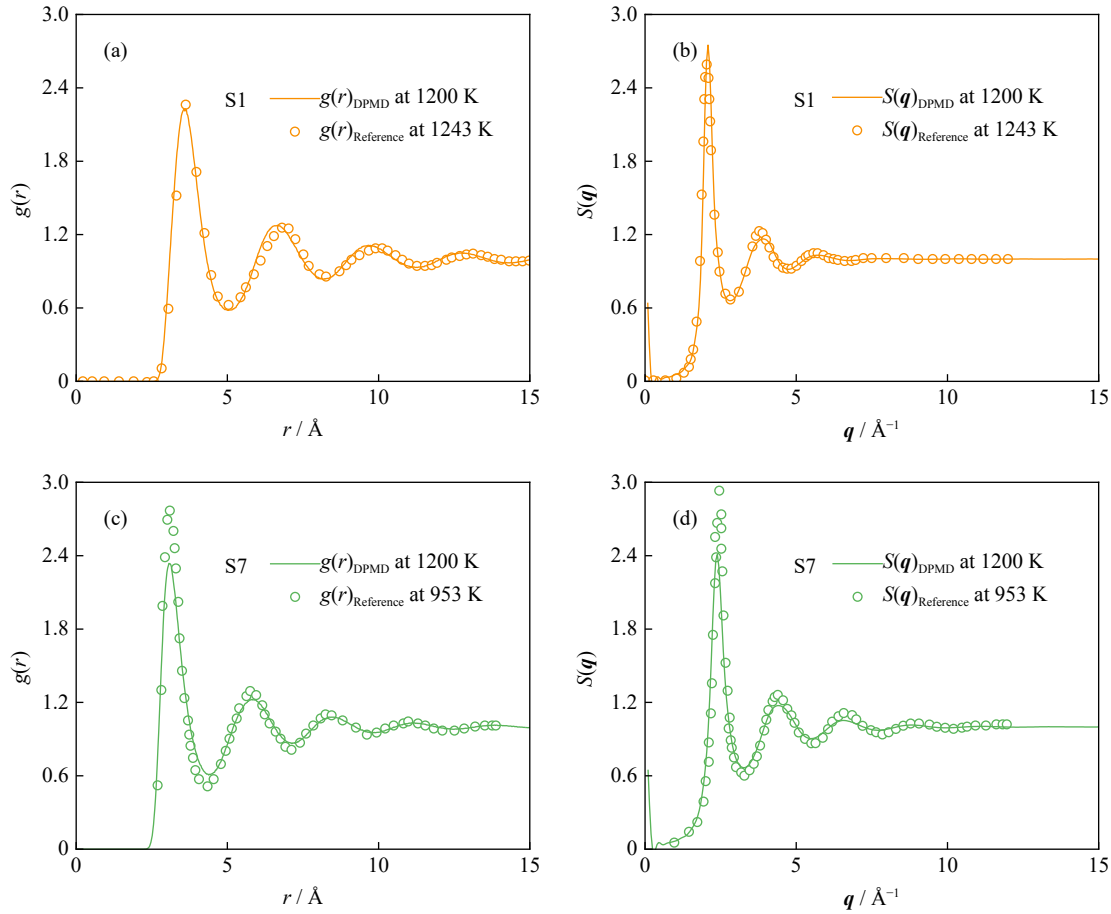

Fig. 2. Comparison results for the (a, c) radial distribution function ($g(r)$) and (b, d) partial structure factor: (a, b) S1; (c, d) S7.

$$g_{\alpha\beta}(r) = \frac{1}{4\pi\rho_\beta r^2}\frac{\mathrm{d}N_{\alpha\beta}(r)}{\mathrm{d}r} \quad (4)$$

where ρ_β is the number density of β atoms, $N_{\alpha\beta}(r)$ is the average number of β atoms with the α ions in the center, and r represents the distance from the reference particle.

Fig. 3 demonstrates the progression of the RDF for Mg–Mg, Mg–La, and La–La with the Mg content in the system at 1200 K. All RDFs display a significant first peak, followed by decreasing fluctuations, finally converging to 1. With increasing Mg content in the system, the first peak position in the RDF of atom pairs changes negligibly, while its heights show a decreasing trend, suggesting that the atomic interaction is weaker for the Mg-rich system. For the other peaks, the variations for Mg–La and La–La are slight, while Mg–Mg exhibits fluctuations.

Fig. 4 shows the progression of RDF of Mg–Mg, Mg–La, and La–La versus temperature (T), which ranges from 1200 to 1800 K for the S4 sample. The shift of the first peak positions of Mg–Mg, Mg–La, and La–La with temperature is negligible, and the detailed data are shown in Table 3, indicating that the temperature effect on the first shell coordination distances of the Mg–La system is slight, as is the change in coordination number. As the temperature increases, all the first peak intensities decay, which is attributed to the increased thermal motion of the atoms at high temperatures and the weakening of the atomic interaction forces.

3.2.2. Structure factor

The intermediate range order of Mg–La liquid alloy was investigated through the structure factor, which could be expressed as Eq. (5) [44].

$$S_{\alpha\beta}(\boldsymbol{q}) = 1 + 4\pi\int_0^\infty r^2\frac{\sin\boldsymbol{q}r}{\boldsymbol{q}r}[g_{\alpha\beta}(r)-1]\mathrm{d}r \quad (5)$$

where $\boldsymbol{q}$ is the wave vector.

Fig. 5(a) illustrates the structure factor of the Mg–La system at 1200 K with different Mg contents. The start position of horizontal coordinates is 0.8 Å^{-1}, which avoids spurious signals due to truncation errors [45]. A distinct first peak is exhibited among all components, implying the presence of a short-range ordered structure in the system. As the Mg content increases, the intensity of the first peak weakens and shifts to the right, and the distance between the atoms in real space decreases, which could be attributed to the smaller atomic radius of Mg. Furthermore, there is a small peak around 1.30 Å^{-1} observed in Fig. 5 (inset), indicating the presence of an intermediate-range ordered structure within the melt, which is particularly pronounced in the S6 sample. This indicates that 80at% of the Mg in the system may prefer to form compounds or atom clusters [46].

To discuss the temperature relationship of the structure factor in the Mg–La liquid alloy, Fig. 5(b) depicts the evolution of the structure factor over temperature for the S6 sample. The intensity of the first peak decreases as the temperature increases, suggesting that the short-range order is decreasing. Meanwhile, the peak position of the first peak is shifted to the left, demonstrating that the thermal motion is intensified at high temperatures, which is reflected in the larger spacing between the atoms in real space compared to low temperatures. Furthermore, the pre-peak intensity is weakened, becoming slight at 1400 K and negligible at 1600 K. This indicates that the increase in temperature yields the disappearance of the intermediate range ordered in the melt,

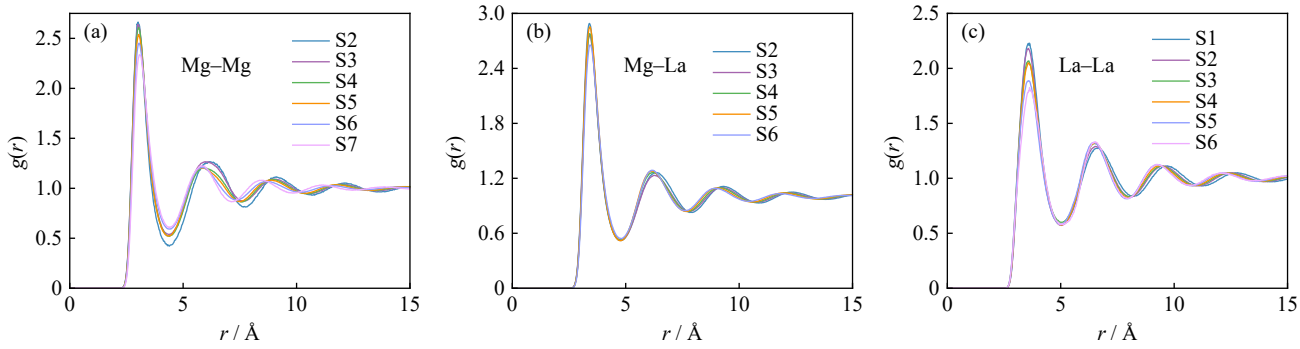

Fig. 3. Evolution pattern of RDF for (a) Mg–Mg, (b) Mg–La, and (c) La–La with increasing Mg content in the system at 1200 K.

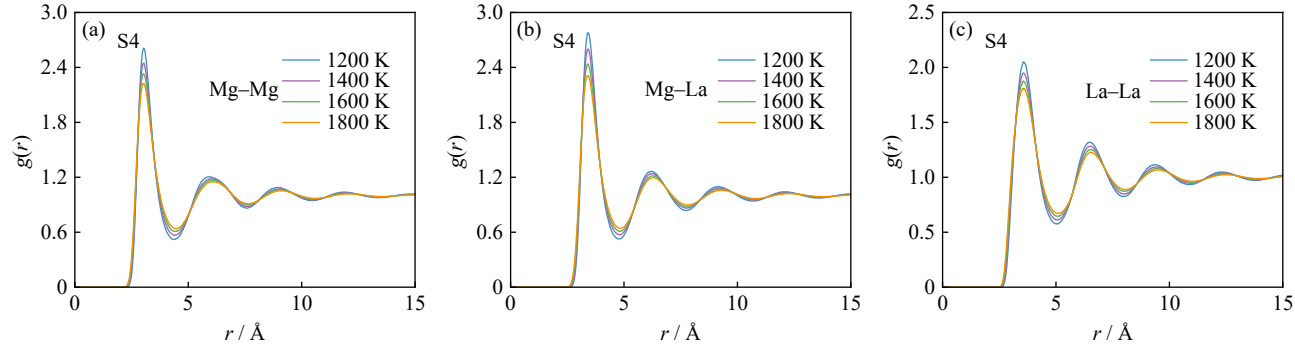

Fig. 4. Temperature relationship of the RDF for the S4 sample from 1200 to 1800 K: (a) Mg–Mg, (b) Mg–La, and (c) La–La.

Table 3. Position of the first peak (r_{max}), its height (h_{max}), and coordination number ($N_{\alpha\beta}$) of Mg–Mg, Mg–La, and La–La for all samples in the Mg–La liquid alloy system from 1200 to 1800 K with 200 K intervals

System	T / K	Mg–Mg			Mg–La			La–La		
		r_{max} / Å	h_{max}	$N_{\alpha\beta}$	r_{max} / Å	h_{max}	$N_{\alpha\beta}$	r_{max} / Å	h_{max}	$N_{\alpha\beta}$
S1	1200							3.57	2.22	13.93
	1400							3.58	2.11	13.79
	1600							3.57	2.02	13.91
	1800							3.53	1.94	13.61
S2	1200	3.01	2.66	1.80	3.41	2.89	10.47	3.57	2.18	11.41
	1400	3.00	2.56	1.86	3.37	2.66	10.28	3.56	2.06	11.43
	1600	3.01	2.44	1.97	3.41	2.50	10.30	3.58	1.97	11.44
	1800	2.98	2.38	1.96	3.38	2.38	10.24	3.54	1.89	11.33
S3	1200	3.00	2.64	4.07	3.41	2.76	8.12	3.60	2.07	9.00
	1400	3.02	2.48	4.12	3.41	2.59	8.06	3.57	1.97	9.09
	1600	3.01	2.39	4.18	3.40	2.42	7.97	3.56	1.90	8.96
	1800	3.02	2.27	4.12	3.39	2.31	7.87	3.56	1.84	9.21
S4	1200	3.04	2.61	5.25	3.42	2.78	7.06	3.58	2.05	7.59
	1400	3.03	2.45	5.21	3.42	2.60	6.97	3.57	1.95	7.60
	1600	3.02	2.33	5.23	3.41	2.44	7.02	3.57	1.88	7.70
	1800	3.04	2.23	5.34	3.43	2.31	6.86	3.52	1.81	7.48
S5	1200	3.04	2.54	6.39	3.42	2.85	5.88	3.57	1.89	5.96
	1400	3.04	2.39	6.43	3.42	2.64	5.81	3.57	1.82	6.06
	1600	3.03	2.28	6.27	3.39	2.47	5.69	3.55	1.76	6.11
	1800	3.05	2.19	6.35	3.41	2.33	5.73	3.57	1.72	6.09
S6	1200	3.06	2.45	9.58	3.43	2.66	3.15	3.63	1.83	3.37
	1400	3.04	2.30	9.50	3.41	2.47	3.14	3.63	1.78	3.31
	1600	3.06	2.18	9.40	3.42	2.32	3.03	3.55	1.75	3.33
	1800	3.04	2.10	9.20	3.42	2.28	2.99	3.55	1.59	3.05
S7	1200	3.06	2.34	12.67						
	1400	3.10	2.20	12.47						
	1600	3.03	2.09	12.54						
	1800	3.05	2.01	12.64						

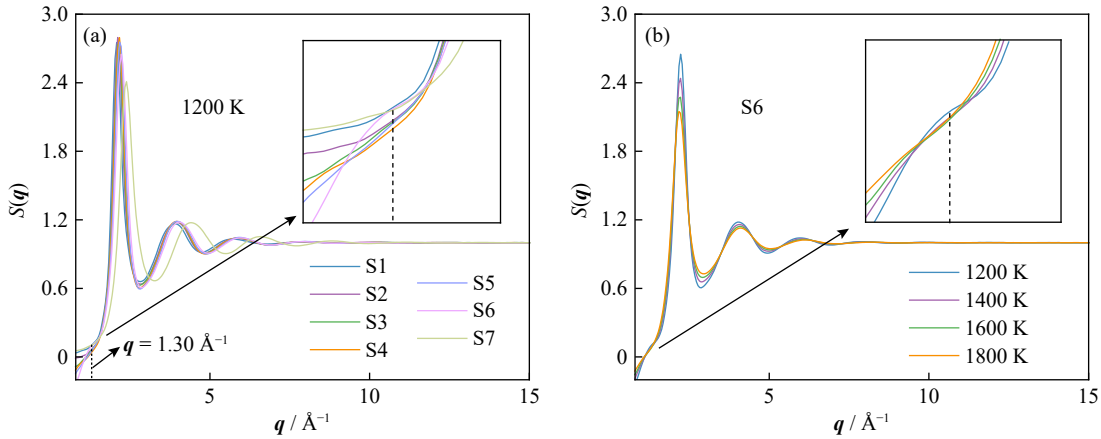

Fig. 5. (a) Structure factor of the Mg–La system at 1200 K; (b) evolution of structure factor with temperature for the S6 sample.

and the Mg–La liquid alloy exhibits only the short-range ordered at high temperatures.

3.3. Macroscopic properties

3.3.1. Density

The density of the liquid metal is required for calculating the conservation of mass during refinement operations, and it is also used as a key input parameter for deriving other thermophysical behavior in the casting and solidifying processes. The density of all samples was evaluated by Eq. (6) [43].

$$\rho = \frac{\sum_i N_i M_i}{V_E N_A} \tag{6}$$

where ρ is the density of the sample, N_i represents the atomic number, M_i denotes the molar mass of the corresponding

atom, V_E is the equilibrium volume, and N_A is Avogadro's constant.

Fig. 6 shows the densities derived from the DPMD simulations as well as the experimental values for S1 [47] and S7 [48], and the presented values for S2 to S6 were deduced based on the densities of Mg and La, which were calculated by ignoring the volume changes during the mixing process. The maximum relative density error is 6.32% for S1 at 1800 K, which is higher in the La-rich system due to the larger RMSEs shown in Section 3.1 when testing the trained DP model. Overall, this is acceptable for the Mg–La liquid alloy.

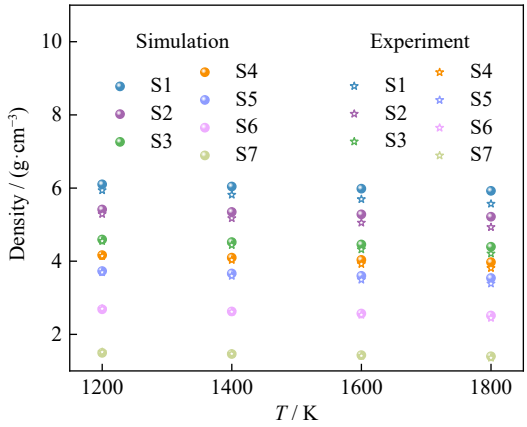

Fig. 6. Evolution pattern of density of Mg–La liquid alloy with temperature for all samples.

As the temperature increases, owing to the higher average kinetic energy of its atoms, the interaction between them is weakened, resulting in an increase in the atomic distance, leading to a decrease in the atomic number of the unit volume and a decrease in the density of the system. With increasing magnesium content, the density of the Mg–La liquid alloy decreases because the density of Mg is much lower than that of La. As a result, the density database of the Mg–La system, containing different Mg content from 1200 to 1800 K, was constructed.

3.3.2. Self-diffusion coefficient

In this work, the self-diffusion coefficient of the Mg–La alloy system is derived from the DPMD simulation based on the Einstein-Smoluchowski equation [43], as shown in Eq. (7).

$$D = \frac{1}{6}\lim_{t\to\infty}\frac{\mathrm{d(MSD)}}{\mathrm{d}t} = \frac{1}{6}\lim_{t\to\infty}\frac{\mathrm{d}\left(\frac{1}{N}\left\langle\sum_i |r_i(t)-r_i(0)|^2\right\rangle\right)}{\mathrm{d}t} \quad (7)$$

where MSD is the mean square displacement, $r_i(t)$ is the displacement of the i atom at time t.

For sample S4, the dependence between the self-diffusion coefficients of Mg and La with temperature is displayed in Fig. 7(a). It is shown that the self-diffusion coefficients of Mg and La increase with increasing temperature. The self-diffusion coefficients of Mg are larger than those of La. The self-diffusion coefficient increases from 4.33×10^{-5} to 10.74×10^{-5} cm^2/s for Mg from 1200 to 1800 K, while for La, it is from 3.26×10^{-5} to 10.11×10^{-5} cm^2/s. Moreover, the evolution of the natural logarithm of the self-diffusion coefficient with the temperature inverse for S4 is shown in Fig. 7(b), and their relationship is linearly expressed as Eqs. (8-1) and (8-2), where R represents the gas constant. The corresponding diffusion activation energies are obtained. For Mg, E_a is 28.31 kJ/mol, while for La, it is 33.12 kJ/mol.

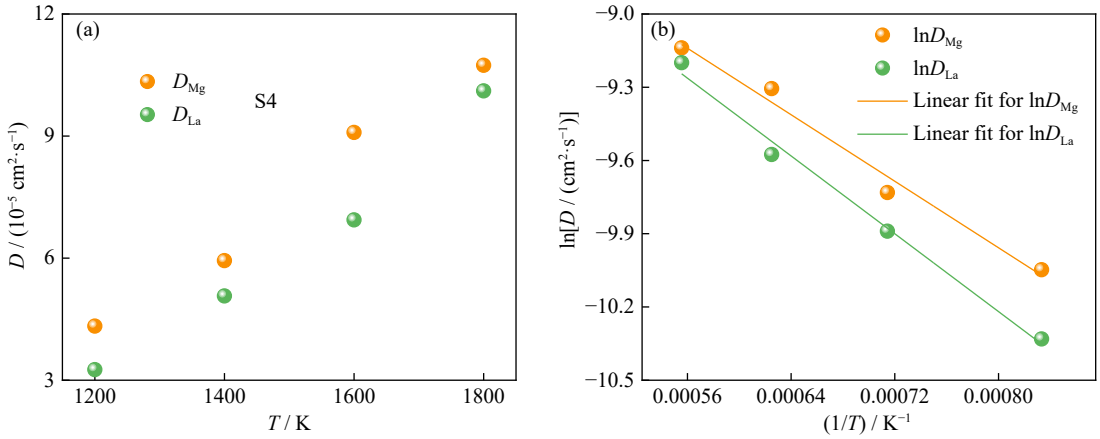

Fig. 7. (a) Temperature evolution of the self-diffusion coefficients of Mg and La for the S4 sample; (b) natural logarithm of the self-diffusion coefficients with the inverse of the temperature.

$$\ln D_{Mg} = -7.23 - 28305.56/(RT) \quad (8\text{-}1)$$

$$\ln D_{La} = -7.03 - 33120.42/(RT) \quad (8\text{-}2)$$

The self-diffusion coefficients of the other systems are presented in Fig. 8. The self-diffusion coefficients of both Mg and La show an increasing trend with increasing Mg content in the system due to the smaller atomic size of Mg, which contributes to a lower resistance to spatial motion. Furthermore, the self-diffusion coefficient of Mg reported by S.D. Korkmaz and Ş. Korkmaz is 6.64×10^{-5} cm^2/s at 953 K [49]. In this work, based on the temperature dependence of the self-diffusion coefficient in Fig. 8(f), the self-diffusion coefficient of Mg at 953 K is predicted to be 5.69×10^{-5} cm^2/s using the Arrhenius law. This value is close to the reference, indicating the reliability of our calculations.

3.3.3. Shear viscosity

The shear viscosity is derived from the self-diffusion coefficient based on the Stokes-Einstein equation [50], as shown

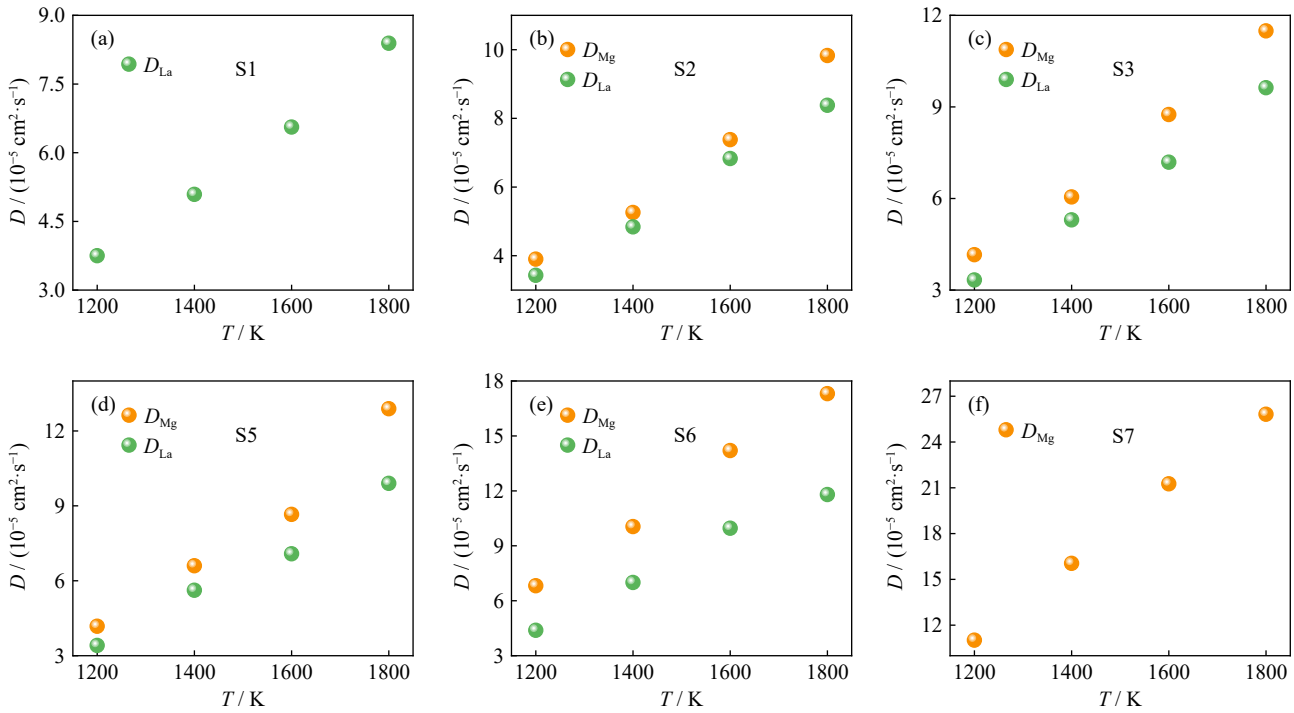

Fig. 8. Self-diffusion coefficient for (a–f) S1 to S7, except S4, covering the temperature from 1200 to 1800 K.

in Eq. (9).

$$\eta_{SE} = \frac{k_B T}{2\pi \overline{D} R_s} \tag{9}$$

where k_B is the Boltzmann constant taken as 1.38×10^{-23} J/K, and $\overline{D}$ is the arithmetic average of D_{Mg} and D_{La}. R_s is the solvodynamic mean radius of the system, the detailed expression of which, referring to the combination rule reported in the literature [51], is shown in Eq. (10), Eq. (11), and Eq. (12) for the S1 system, S2–S6 systems, and S7 system, respectively.

For S1 system:

$$R_s = d_{La\text{–}La} \tag{10}$$

For S2–S6 system:

$$R_s = \frac{d_{Mg\text{–}Mg} + d_{La\text{–}La} + 2d_{Mg\text{–}La}}{4} \tag{11}$$

For S7 system:

$$R_s = d_{Mg\text{–}Mg} \tag{12}$$

The $d_{Mg\text{–}Mg}$ and $d_{La\text{–}La}$ in Eqs. (10), (11), and (12) represent the effective atomic diameter, considered as the first peak position of the RDF as listed in Table 3. Fig. 9 presents the progression of shear viscosity with temperature from 1200 to 1800 K for all samples in Mg–La liquid alloy. It is shown that the viscosity of each sample decreases with increasing temperature. This phenomenon is due to enhanced atom motion and weakened atomic interactions, thus reducing the mutual obstruction between atoms. For S1, the shear viscosity decreased from 1.97 to 1.34 mPa·s, which is slightly lower than the value reported by Patel *et al.* [52] (2.58 mPa·s). While for S7, it decreases from 0.78 to 0.50 mPa·s from 1200 to 1800 K. The viscosity at 953 K is deduced from its temperature dependence to be 1.09 mPa·s, which agrees well with 1.25 mPa·s at 953 K reported by Yokoyama and Tsuchiya [53] for liquid Mg. Although the change pattern in the shear viscosity is not pronounced for the La-rich system, the viscosity generally exhibits a decreasing trend with increasing Mg content over the whole concentration range. This observation could be attributed to greater motion resistance due to stronger interaction in the La-rich system.

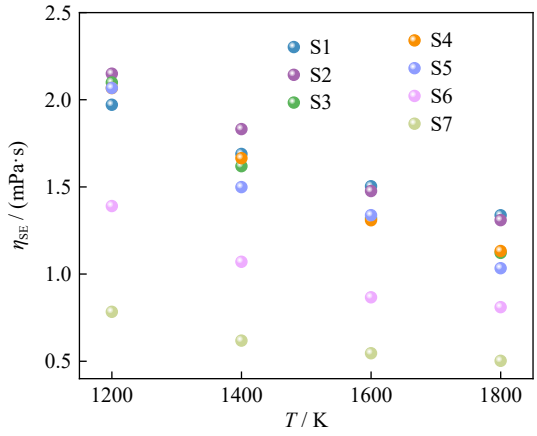

Fig. 9. Evolution of shear viscosity from 1200 to 1800 K, derived from DPMD simulation, for all samples in the Mg–La liquid alloy.

3.4. Thermodynamic behavior analysis

This work assessed the mixing enthalpy of the Mg–La liquid alloy system at 1200 K via Eq. (13) [54]. The results for all the samples are shown in Fig. 10(a). All the enthalpies of mixing from S2 to S6 are negative, indicating that the Mg and La atoms are attracted to each other and the alloy is fully mixed in the liquid state. The mixing enthalpy decreases with

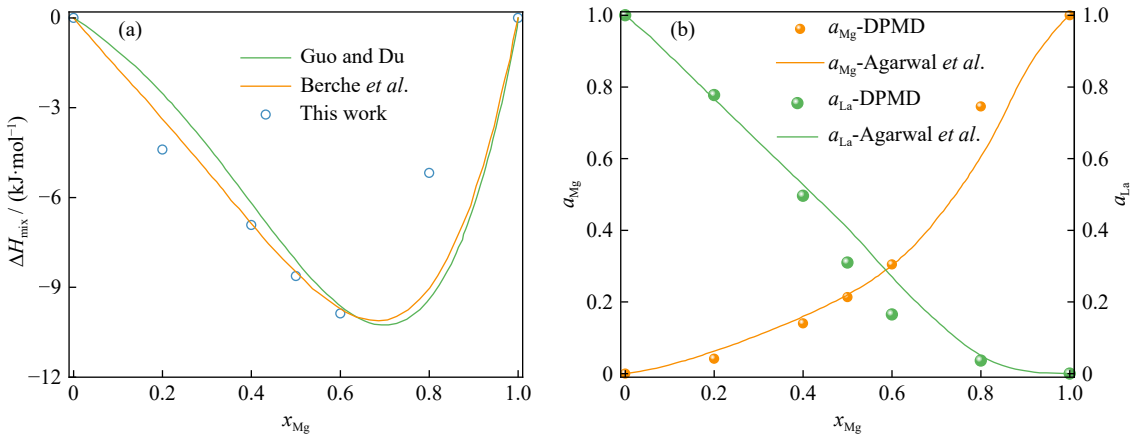

Fig. 10. (a) Evolution of the mixing enthalpy for the Mg–La liquid alloy system; (b) activity of Mg and La in Mg–La liquid alloy.

increasing Mg content in the Mg–La system and reaches its minimum at x_{Mg} = 0.6 (mole ratio), after which ΔH_{mix} increases with increasing Mg content. The mixing enthalpy curves show an asymmetry, with the minimum value favoring the Mg side, and the overall trend of the evolution of the mixing enthalpy with x_{Mg} agrees well with that reported in the literature. In detail, the predicted mixing enthalpies from S2 to S5 by the DP model agrees well with those reported by Berche *et al.* [55] at 1031 K and Guo and Du [7] at 1060 K. However, for S6, i.e., 80at% Mg in the Mg–La system, there is some deviation between the predicted and literature values.

$$\Delta H_{mix} = E_x - [xE_{Mg} + (1-x)E_{La}] \tag{13}$$

where ΔH_{mix} is the mixing enthalpy, E_x represents the energy value of the Mg–La alloy system when the Mg mole ratio is x, E_{Mg} represents the energy of Mg in the same state, and E_{La} is the energy of the corresponding La.

The activity reflects the effective concentration of the system, which is the product of the concentration and the activity coefficient and is of great importance in metallurgy. In this work, the activities of Mg and La in the Mg–La liquid alloy system were determined according to Eqs. (14) and (15), derived from ΔH_{mix}. The dependence of the activities (a) on the Mg content in the Mg–La system is demonstrated in Fig. 10(b). It is observed that the downward concave shape deviates from Raoul's law and forms a negative deviation, indicating that the force of different atoms in the Mg–La liquid system is stronger than that of the same atoms. The activity data have been compared with the results by Agarwal *et al.* at 1133 K [56] using calorimetric measurements. The overall trend in the variation of activity with x_{Mg} is consistent, with slight deviations in the individual components. Overall, it is acceptable.

$$\ln\gamma_{Mg} = \frac{1-0.1\times T\times(1/T_{m\text{-}Mg}+1/T_{m\text{-}La})}{RT}\times \left[\Delta H_{mix} + (1-x_{Mg})\frac{\partial \Delta H_{mix}}{\partial x_{Mg}}\right] \tag{14}$$

$$\ln\gamma_{La} = \frac{1-0.1\times T\times(1/T_{m\text{-}Mg}+1/T_{m\text{-}La})}{RT}\times \left[\Delta H_{mix} + (1-x_{La})\frac{\partial \Delta H_{mix}}{\partial x_{La}}\right] \tag{15}$$

where γ_{Mg} and γ_{La} represent the activity coefficients of Mg and La, respectively; T is the temperature of the study; R is the ideal gas constant; $T_{m\text{-}La}$ is the melting point of La, and $T_{m\text{-}Mg}$ is the melting point of Mg; x_{Mg} and x_{La} represent the mole fractions of Mg and La in the liquid alloy, respectively.

Due to the challenges of determining activity data at high temperatures, researchers have attempted to establish activity predictions by coupling statistical thermodynamics through structural modeling of the components with each other, but these are often limited in their applicability. This reliable work suggests that the application of DPMD simulation driven by machine learning may provide new ideas and guidance for the rapid and accurate establishment of activity expression relationships for alloy systems.

4. Conclusions

The Mg–La liquid alloy was thoroughly understood from local structure, macroscopic properties, and thermodynamic behavior.

Firstly, the accuracy of the trained DP model was validated by RMSEs, for energy, it is 6.70 meV/atom, while for force, it is 0.14 eV/Å. The comparison results of RDF and partial structure factor further illustrated that the DP model is well-trained.

Secondly, the dependence of the local structure of the Mg–La liquid alloy on temperature and composition changes was systematically investigated, and it was confirmed that the system is not only short-range ordered but also intermediate-range ordered, particularly pronounced in the S6 (80at% Mg) sample. The temperature evolution of the first peak intensity of RDF is consistent with that of the Mg content in the system. At high temperatures, the Mg–La liquid alloy shows only short-range ordering.

Subsequently, the macroscopic properties of the system were discussed, and the corresponding property database of the Mg–La liquid alloy with different Mg contents from 1200 to 1800 K was constructed. Their temperature and component dependencies were elucidated. The self-diffusion coefficients of Mg and La at different temperatures follow the Arrhenius formula, and the diffusion activation energies for the S4 sample are then derived; for Mg, E_a is 28.31 kJ/mol,

while for La, it is 33.12 kJ/mol.

Finally, the thermodynamic behavior of the Mg–La alloy was evaluated at 1200 K. The mixing enthalpies for S2 to S6 are negative, indicating that the Mg and La atoms are attracted to each other and the alloy is fully mixed in the liquid state. The dependence of the Mg and La activities on the Mg content shows a downward concave shape that deviates from Raoul's law and forms a negative deviation. Moreover, the reliable results demonstrate that DPMD simulation could offer new guidance for related studies.

Acknowledgement

This work was financially supported by the National Key R&D Program of China (No. 2022YFB3709300).

Conflict of Interest

The authors declare that they have no known competing financial interests or personal relationships, as shown in this paper.

References

[1] T. Takenaka, T. Ono, Y. Narazaki, Y. Naka, and M. Kawakami, Improvement of corrosion resistance of magnesium metal by rare earth elements, *Electrochim. Acta*, 53(2007), No. 1, p. 117.

[2] L.B. Tong, Q.X. Zhang, Z.H. Jiang, *et al*., Microstructures, mechanical properties and corrosion resistances of extruded Mg–Zn–Ca–*x*Ce/La alloys, *J. Mech. Behav. Biomed. Mater.*, 62(2016), p. 57.

[3] Q.X. Zhang, L.B. Tong, L.R. Cheng, Z.H. Jiang, J. Meng, and H.J. Zhang, Effect of Ce/La microalloying on microstructural evolution of Mg–Zn–Ca alloy during solution treatment, *J. Rare Earths*, 33(2015), No. 1, p. 70.

[4] J. Rong, J.N. Zhu, W.L. Xiao, X.Q. Zhao, and C.L. Ma, A high pressure die cast magnesium alloy with superior thermal conductivity and high strength, *Intermetallics*, 139(2021), art. No. 107350.

[5] A. Gökçe, Metallurgical assessment of novel Mg–Sn–La alloys produced by high-pressure die casting, *Met. Mater. Int.*, 26(2020), No. 7, p. 1036.

[6] Y.C. Tsai, C.Y. Chou, S.L. Lee, C.K. Lin, J.C. Lin, and S.W. Lim, Effect of trace La addition on the microstructures and mechanical properties of A356 (Al–7Si–0.35Mg) aluminum alloys, *J. Alloys Compd.*, 487(2009), No. 1-2, p. 157.

[7] C.P. Guo and Z.M. Du, Thermodynamic assessment of the La–Mg system, *J. Alloys Compd.*, 385(2004), No. 1-2, p. 109.

[8] M.Y. Li, S.Z. Du, R.X. Liu, S.J. Lu, P. Jia, and H.R. Geng, Local structure and its change of Al–Ni alloy melts, *J. Mol. Liq.*, 200(2014), p. 168.

[9] P. Srirangam, M.J. Kramer, and S. Shankar, Effect of strontium on liquid structure of Al–Si hypoeutectic alloys using high-energy X-ray diffraction, *Acta Mater.*, 59(2011), No. 2, p. 503.

[10] C. Notthoff, B. Feuerbacher, H. Franz, D.M. Herlach, and D. Holland-Moritz, Direct determination of metastable phase diagram by synchrotron radiation experiments on undercooled metallic melts, *Phys. Rev. Lett.*, 86(2001), No. 6, p. 1038.

[11] Y.B. Wang, S.S. Jia, M.G. Wei, L.M. Peng, Y.J. Wu, and X.T. Liu, Research progress on solidification structure of alloys by synchrotron X-ray radiography: A review, *J. Magnes. Alloys*, 8(2020), No. 2, p. 396.

[12] L.F. Zhang, H. Wang, R. Car, and Weinan E, Phase diagram of a deep potential water model, *Phys. Rev. Lett.*, 126(2021), No. 23, art. No. 236001.

[13] J.Z. Zeng, L.Q. Cao, M.Y Xu, T. Zhu, and J.Z.H. Zhang, Complex reaction processes in combustion unraveled by neural network-based molecular dynamics simulation, *Nat. Commun.*, 11(2020), No. 1, art. No. 5713.

[14] M.Y. Yang, U. Raucci, and M. Parrinello, Reactant-induced dynamics of lithium imide surfaces during the ammonia decomposition process, *Nat. Catal.*, 6(2023), No. 9, p. 829.

[15] J.C. Liu, L.L. Luo, H. Xiao, J.F. Zhu, Y. He, and J. Li, Metal affinity of support dictates sintering of gold catalysts, *J. Am. Chem. Soc.*, 144(2022), No. 45, p. 20601.

[16] J.Y. Jiao, G.M. Lai, L. Zhao, *et al*., Self-healing mechanism of lithium in lithium metal, *Adv. Sci.*, 9(2022), No. 12, art. No. 2105574.

[17] J. Zhao, T.X. Feng, G.M. Lu, and J.G. Yu, Insights into the local structure evolution and thermophysical properties of NaCl–KCl–$MgCl_2$–$LaCl_3$ melt driven by machine learning, *J. Mater. Chem. A*, 11(2023), No. 44, p. 23999.

[18] T.R. Xu, X.J. Li, Y. Wang, and Z.F. Tang, Development of deep potentials of molten $MgCl_2$–NaCl and $MgCl_2$–KCl salts driven by machine learning, *ACS Appl. Mater. Interfaces*, 15(2023), No. 11, p. 14184.

[19] C.S. Zhu, W.J. Dong, Z.H. Gao, L.J. Wang, and G.Z. Li, Deep Potential fitting and mechanical properties study of MgAlSi alloy, *Comput. Mater. Sci.*, 239(2024), art. No. 112966.

[20] N. Xu, Y. Shi, Y. He, and Q. Shao, A deep-learning potential for crystalline and amorphous Li–Si alloys, *J. Phys. Chem. C*, 124(2020), No. 30, p. 16278.

[21] Q. Wang, B. Zhai, H.P. Wang, and B. Wei, Atomic structure of liquid refractory Nb_5Si_3 intermetallic compound alloy based upon deep neural network potential, *J. Appl. Phys.*, 130(2021), No. 18, art. No. 185103.

[22] T.Q. Wen, C.Z. Wang, M.J. Kramer, *et al*., Development of a deep machine learning interatomic potential for metalloid-containing Pd–Si compounds, *Phys. Rev. B*, 100(2019), No. 17, art. No. 174101.

[23] B. Zhai and H.P. Wang, Accurate interatomic potential for the nucleation in liquid Ti–Al binary alloy developed by deep neural network learning method, *Comput. Mater. Sci.*, 216(2023), art. No. 111843.

[24] R.E. Ryltsev and N.M. Chtchelkatchev, Deep machine learning potentials for multicomponent metallic melts: Development, predictability and compositional transferability, *J. Mol. Liq.*, 349(2022), art. No. 118181.

[25] L. Tang, Z.J. Yang, T.Q. Wen, K.M. Ho, M.J. Kramer, and C.Z. Wang, Development of interatomic potential for Al–Tb alloys using a deep neural network learning method, *Phys. Chem. Chem. Phys.*, 22(2020), No. 33, p. 18467.

[26] L. Tang, K.M. Ho, and C.Z. Wang, Molecular dynamics simulation of metallic Al-Ce liquids using a neural network machine learning interatomic potential, *J. Chem. Phys.*, 155(2021), No. 19, art. No. 194503.

[27] X. He, J.D. Liu, C. Yang, and G. Jiang, Predicting thermodynamic stability of magnesium alloys in machine learning, *Comput. Mater. Sci.*, 223(2023), art. No. 112111.

[28] Y.N. Wang, X.Y. Wang, W.R. Jiang, H. Wang, and F.Z. Dai, Domain structures and stacking sequences of Mg–Zn–Y long-period stacking ordered (LPSO) structures predicted by deep-learning potential, *Mater. Today Commun.*, 38(2024), art. No. 108301.

[29] W.R. Jiang, Y.Z. Zhang, L.F. Zhang, and H. Wang, Accurate deep potential model for the Al–Cu–Mg alloy in the full concentration space, *Chin. Phys. B*, 30(2021), No. 5, art. No. 050706.

[30] H.D. Wang, Y.Z. Zhang, L.F. Zhang, and H. Wang, Crystal

structure prediction of binary alloys via deep potential, *Front. Chem.*, 8(2020), art. No. 589795.
[31] C.H. Li, H.L. Zhang, D.L. Guo, and W. Zeng, Crystal structure prediction and property calculation of Al_2CuMg by deep learning potential, *J. Mater. Eng. Perform.*, (2023). https://doi.org/10.1007/s11665-023-08944-9
[32] G. Kresse and J. Furthmüller, Efficient iterative schemes for ab initio total-energy calculations using a plane-wave basis set, *Phys. Rev. B*, 54(1996), No. 16, p. 11169.
[33] G. Kresse and D. Joubert, From ultrasoft pseudopotentials to the projector augmented-wave method, *Phys. Rev. B*, 59(1999), No. 3, p. 1758.
[34] J.P. Perdew, K. Burke, and M. Ernzerhof, Generalized gradient approximation made simple, *Phys. Rev. Lett.*, 77(1996), No. 18, p. 3865.
[35] S. Grimme, J. Antony, S. Ehrlich, and H. Krieg, A consistent and accurate *ab initio* parametrization of density functional dispersion correction (DFT-D) for the 94 elements H–Pu, *J. Chem. Phys.*, 132(2010), No. 15, art. No. 154104.
[36] Y.Z. Zhang, H.D. Wang, W.J. Chen, *et al*., DP-GEN: A concurrent learning platform for the generation of reliable deep learning based potential energy models, *Comput. Phys. Commun.*, 253(2020), art. No. 107206.
[37] L.F. Zhang, J.Q. Han, H. Wang, R. Car, and Weinan E, Deep potential molecular dynamics: A scalable model with the accuracy of quantum mechanics, *Phys. Rev. Lett.*, 120(2018), No. 14, art. No. 143001.
[38] L. Zhang, J. Han, H. Wang, W.A. Saidi, R. Car, and Weinan E, End-to-end symmetry preserving inter-atomic potential energy model for finite and extended systems, [in] *Proceedings of the 32nd Conference on Neural Information Processing Systems*, Montréal, 2018, p. 4441.
[39] S. Plimpton, Fast parallel algorithms for short-range molecular dynamics, *J. Comput. Phys.*, 117(1995), No. 1, p. 1.
[40] S.L. Roux and P. Jund, Ring statistics analysis of topological networks: New approach and application to amorphous GeS_2 and SiO_2 systems, *Comput. Mater. Sci.*, 49(2010), No. 1, p. 70.
[41] S. Dalgic, S. Dalgic, S. Sengul, M. Celtek, and G. Tezgor, Liquid structure of some rare-earth metals using an analytic pair potential, *J. Optoelectron. Adv. Mater.*, 3(2001), No. 4, p. 831.
[42] J.F. Wax, R. Albaki, and J.L. Bretonnet, Structural and dynamical properties of liquid alkaline-earth metals near the melting point, *Phys. Rev. B*, 62(2000), No. 22, p. 14818.
[43] J. Wang, Z. Sun, G. Lu, and J. Yu, Molecular dynamics simulations of the local structures and transport coefficients of molten alkali chlorides, *J. Phys. Chem. B*, 118(2014), No. 34, p. 10196.
[44] T.E. Faber and J.M. Ziman, A theory of the electrical properties of liquid metals, *Philos. Mag.*, 11(1965), No. 109, p. 153.
[45] H.T. Reijers, W. van der Lugt, and M.L. Saboungi, Molecular-dynamics study of liquid NaPb, KPb, RbPb, and CsPb alloys, *Phys. Rev. B.*, 42(1990), No. 6, p. 3395.
[46] S. Takeda, S. Harada, S. Tamaki, E. Matsubara, and Y. Waseda, Structural study of liquid Na–Pb alloys by neutron diffraction, *J. Phys. Soc. Jpn.*, 56(1987), No. 11, p. 3934.
[47] V.I. Kohonenko, A.L. Sukhman, S.L. Gruverman, and V.V. Torokin, Density and surface tension of liquid rare earth metals, scandium, and yttrium, *Phys. Status Solidi A*, 84(1984), No. 2, p. 423.
[48] P.J. McGonigal, A.D. Kirshenbaum, and A.V. Grosse, The liquid temperature range, density, and critical constants of magnesium, *J. Phys. Chem.*, 66(1962), No. 4, p. 737.
[49] S.D. Korkmaz and Ş. Korkmaz, Atomic transport properties of liquid alkaline earth metals: A comparison of scaling laws proposed for diffusion and viscosity, *Modelling Simul. Mater. Sci. Eng.*, 15(2007), No. 3, p. 285.
[50] R. Vuilleumier, A. Seitsonen, N. Sator, and B. Guillot, Structure, equation of state and transport properties of molten calcium carbonate ($CaCO_3$) by atomistic simulations, *Geochim. Cosmochim. Acta*, 141(2014), p. 547.
[51] X.J. Li, J. Song, S.P. Shi, *et al*., Dynamic fluctuation of U^{3+} coordination structure in the molten LiCl–KCl eutectic *via* first principles molecular dynamics simulations, *J. Phys. Chem. A*, 121(2017), No. 3, p. 571.
[52] H.P. Patel, Y.A. Sonvane, P.B. Thakor, and A.V. Prajapati, Shear viscosity coefficient of liquid lanthanides, *AIP Conf. Proc.*, 1661(2015), No. 1, art. No. 110012.
[53] I. Yokoyama and S. Tsuchiya, Excess entropy, diffusion coefficient, viscosity coefficient and surface tension of liquid simple metals from diffraction data, *Mater. Trans.*, 43(2002), No. 1, p. 67.
[54] T.T. Xu, J.Y. Li, R.L. Xiao, J.Y. Qin, Y. Ruan, and H. Li, The mixing enthalpy and liquid structural properties of Ti–Al alloys by ab inito molecular dynamics simulation, *J. Phase Equilib. Diffus.*, 43(2022), No. 5, p. 585.
[55] A. Berche, P. Benigni, J. Rogez, and M.C. Record, Thermodynamic assessment of the La–Mg system, *Calphad*, 35(2011), No. 4, p. 580.
[56] R. Agarwal, H. Feufel, and F. Sommer, Calorimetric measurements of liquid La–Mg, Mg–Yb and Mg–Y alloys, *J. Alloys Compd.*, 217(1995), No. 1, p. 59.